Optics Letters

Transient wind camera using 1(seed) × 10(amplifier) CDWL with a frame rate of 2 Hz and a range of 5 km

JINLONG YUAN,^{1,2,3} JIAWEI QIU,³ JIADONG HU,³ JIANJUN HU,⁴ AND HAIYUN XIA^{1,3,5,6,*}

- ¹ State Key Laboratory of Climate System Prediction and Risk Management, NUIST, Nanjing 210044, China
- ²Weather Modification Centre, China Meteorological Administration, Beijing 100081, China
- ³ School of Atmospheric Physics, Nanjing University of Information Science and Technology, Nanjing 210044, China
- ⁴School of Optoelectronic Science and Engineering, Soochow University, Suzhou 215006, China
- ⁵School of Earth and Space Science, University of Science and Technology of China, Hefei 230026, China
- ⁶Institute of Lidar Technology, GuangZai Co., Ltd., Hangzhou 310005, China

Received 9 July 2025; revised 5 August 2025; accepted 6 August 2025; posted 13 August 2025; published 27 August 2025

To capture transient wind field information, a multi-beam wind field imaging camera is proposed and validated. Equipped with a 1(seed) × 10(amplifier) transmitter and a single-aperture multi-channel telescope, the new system enables wind imaging at a frame rate of 2 Hz, over a 27° field of view, and within a 5-km detection range. Its performance is validated through comparative experiments against a simulated scanning coherent Doppler wind lidar, which exhibits time lags across individual lines of sight. The transient wind camera eliminates wind measurement errors induced by wind field evolution during the usual scanning cycle. Furthermore, it shows superiority in measuring turbulent spatial spectra. © 2025 Optica Publishing Group. All rights, including for text and data mining (TDM), Artificial Intelligence (Al) training, and similar technologies, are reserved.

https://doi.org/10.1364/OL.573024

Coherent Doppler wind lidar (CDWL) has been widely applied in the detection of atmospheric wind, such as wind shear [1], microburst [2], atmospheric turbulence [3], and aircraft vortices [4]. Highly variable wind fields with drastically changing spatio-temporal velocities can seriously impact aviation safety, meteorological forecasting, structural engineering, wind energy assessment, and so on [5]. The precise detection of highly variable wind fields requires a higher temporal and spatial resolution of CDWL.

In recent years, some new-system lidars have emerged to improve spatial resolution to sub-meter, such as pulse coding [6], differential correlation pair [7], and pseudorandom modulation technique [8]. For the temporal resolution, it mainly relies on increasing the echo signal intensity of a single pulse to reduce pulse accumulation. It can be achieved by increasing pulse power, telescope aperture, and detection efficiency [9,10]. Correspondingly, it will also increase the difficulty of the process and manufacturing costs.

Although great efforts and progress have been made in improving spatio-temporal resolution, the inherent attribute of time-consuming mechanical scanning still exists. Beam switching coherent Doppler wind lidar is optional, mainly for wind

energy applications with short detection range [11]. It requires an optical switch and multiple telescopes and has no more than five beams [12]. Large wind field detection still relies on mechanically scanning lidar. The scanning time and tangential spatial resolution or azimuth resolution are mutually restricted. As a result, the sequential beam sampling mechanism inevitably introduces time-lag effects. It directly leads to low temporal resolution for each scanning cycle. A full field-of-view scan takes several minutes, introducing additional measurement errors and making it difficult to capture rapidly evolving atmospheric phenomena. The two-dimensional (2D) wind field inversion of single Doppler lidar relies on the frozen flow assumption [13,14], and time-lag effects severely affect the inversion accuracy of wind fields. In scenarios with non-uniform wind field evolution, scanning lidars are prone to attenuation of high-frequency turbulence signals due to asynchronous detection times of each beam. Besides, scanning lidars require high-precision motor angle control, and motor failures can cause the entire scanning task to fail. Therefore, the reliable detection of highly variable wind fields remains a challenge.

To overcome time-lag effects, for the first time, a wind camera with 10 measurement channels is designed in this work. By comparing with the results of a simulated scanning wind lidar, its advantages in windshear and turbulence detection are verified.

The system layout of the optical transceiver system is shown in Fig. 1(a). A continuous-wave laser (CWL) at 1550 nm is split into two parts. One portion of the CWL laser is first amplified by a power amplifier and then passed through a 10-channel beam splitter to serve as a local oscillator. The other portion of the CWL as the seed of the transmitted signal is frequency shifted 80 MHz using an acoustic-optic modulator (AOM). The laser bandwidth is 3 kHz, and the power of the CWL is 2 mW. The transmitted signal passes through a 10-channel beam splitter and is amplified by a high-power erbium-doped fiber amplifier (EDFA) array. The amplified lasers are connected to the focal point array on the telescope through a circulator. The backscattered signal of the atmosphere is received through the same telescope. Then, it is mixed with local oscillator light by couplers, which are connected to the detectors array with 10 balance detectors (BDs). The power of the local oscillator on each BD

^{*}hsia@ustc.edu.cn

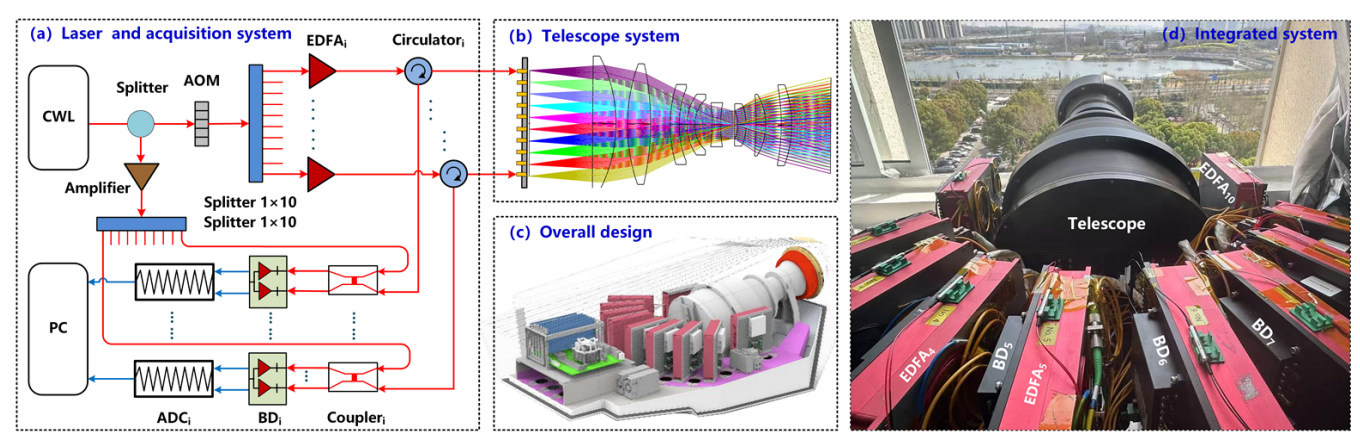


Fig. 1. Diagram of the wind camera. (a) System layout of the laser and acquisition system. ADC, analog-to-digital converter; AOM, acoustic—optic modulator; BD, balance detector; CWL, continuous—wave laser; EDFA, erbium-doped fiber amplifier; PC, personal computer. (b) Schematic diagram of the telescope optical path. (c) Overall design. (d) The integrated system in the experiment.

is 0.8 mW. For the InGaAs PIN diode-based BD, its common-mode rejection ratio (CMRR), responsivity, and bandwidth are >25 dB, >0.8 mA/mW, and 200 MHz, respectively. The optical to electrical signal is acquired by a multi-channel analog-to-digital converter (ADC) array. The ADC array is integrated with an FPGA processor to achieve fast Fourier transform and obtain lidar spectrum.

Figure 1(b) is the diagram of the single-aperture multichannel telescope. The pupil position is close to the third lens of the right. The system uses a classic double-Gauss transmissive symmetric structure as the initial structure. Considering the convenience of fiber alignment, the system is designed to be image-side telecentric, so that the chief rays of the focal plane in each sub-field are parallel to the optical axis of the system. The line-of-sight (LOS) beam waist distance and focal length of the system are 1.39 km and 570 mm, respectively. Its axial length and back focal length measure 673 mm and 162.5 mm, respectively. LOS beam divergence is 44 µrad, with no crosstalk between adjacent channels. The azimuth interval between individual beams is 3°, forming a total field of view of 27°. To improve the transmittance and temperature stability of the optical system, the 10 spherical lenses of the system are all made of Corning 7980-0 F quartz glass.

The overall design of the wind camera is shown in Fig. 1(c). Figure 1(d) is the integrated wind camera system in the experiment. The EDFA array in red is arranged along the telescope. A BD is fixed on the side of each EDFA. The key parameters of the wind camera are summarized in Table 1. The pulse duration and pulse energy of the laser are 200 ns and 100 μ J, respectively. The spatial and temporal resolutions are 30 m and 0.5 s, respectively. The experiment was carried out at the campus of the Nanjing University of Information Science and Technology (32°12′22″N, 118°42′17″E), on 20 March 2025. The lidar system is installed on the ninth floor (altitude of 30 m) of a building, pointing out through a window.

To evaluate the reliability of detection results, the narrowband carrier-to-noise ratio (CNR) [3] and the derived Cramer-Rao lower bound (CRLB) [15] are calculated. The CNR is the ratio of signal power to noise power. CRLB is uncertainties of the measurement, reflecting the accuracy of line-of-sight velocity (LOSV) retrieval. Figure 2 shows the average CNR and corresponding CRLB of 120 frames within 1 min in two cases. There

Table 1. Key Parameters of the Wind Camera

	Parameter	Value
Telescope	Field of view	27°
	Beam divergence	44 μrad
	Telescope diameter	125 mm
	Focal length	570 mm
Laser	Pulse duration	200 ns
	Pulse energy	100 μJ
	Repetition frequency	10 kHz
Receiver	Temporal resolution	0.5 s
	Sample rate	500 MS/s

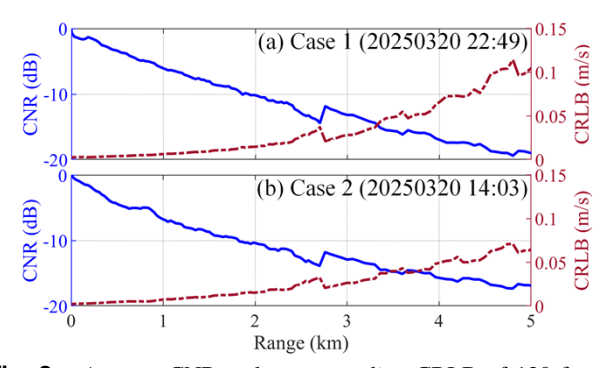


Fig. 2. Average CNR and corresponding CRLB of 120 frames within 1 min. (a) Stable wind field at night. (b) Variable wind field at afternoon.

is an increase of CNR after the range of 2.7 km, because spatial resolution is sacrificed to 60 m for guaranteeing the detection probability at the far field.

For the case of a stable wind field at night, CNR attenuates with distance, and the CNR is not less than $-20\,\mathrm{dB}$ within 5 km, and the corresponding CRLB is less than $0.11\,\mathrm{m/s}$, as shown in Fig. 2(a). For the case of a variable wind field in the afternoon, the CNR is not less than $-18\,\mathrm{dB}$ within 5 km, and the corresponding CRLB is less than $0.07\,\mathrm{m/s}$, as shown in Fig. 2(b). In the afternoon, the temperature is high with abundant aerosol concentration, and the echo intensity is $2\,\mathrm{dB}$ stronger than that at night.

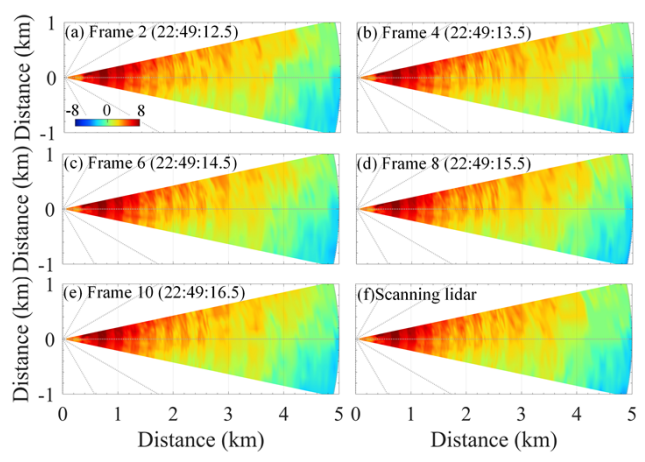


Fig. 3. (a)–(e) Typical imaging results of stable wind field. (f) Corresponding result of scanning lidar.

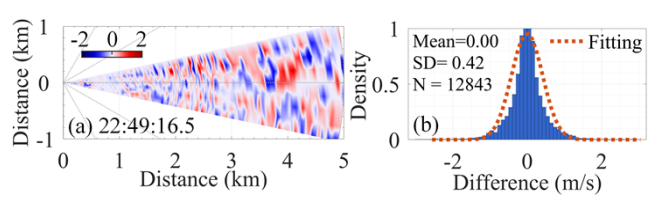


Fig. 4. LOSV difference distribution for the case of stable wind field. (a) LOSV differences between scanning lidar and the wind camera. (b) Probability density distribution of the wind differences.

The wind camera can simultaneously detect the wind field in 10 beam directions, achieving sampling that meets the requirements of wind field freezing. Its detection frequency is 10 times higher than that of traditional mechanical scanning lidar. To enable a valid comparison between this system and the scanning lidar, the line-of-sight direction of each of the 10 beams must be exactly consistent. In this study, 10 beams are sequentially extracted from the 10-frame results of the wind camera to construct the output of the simulated scanning lidar. The velocity expression is as follows:

$$V_s(t) = \{V_C[t + (i-10)dt] \mid i \in (1, 2,10)\},$$
 (1)

where $V_C[t+(i-10)dt]$ represents the wind speed value detected by the ith beam of the wind camera.

Figures 3(a)–3(e) show five-frame LOSV of the imaging results for the case of a stable wind field at 22:49, local time. Due to the effect of the surrounding terrain, a stable band structure is formed. Figure 3(f) shows the constructed result of the scanning lidar, which takes a scanning time of about 5 s. Although the LOSV has reached 8 m/s, the texture structure of the five-frame imaging results is close to that of the scanning results.

Figure 4(a) shows the LOSV difference distribution between the result of the scanning lidar and the first frame result of the wind camera, for the case of a stable wind field. Due to the atmospheric turbulence and movement of aerosol velocity block, the time-lag introduced by the scanning lidar will lead to the method error with a random spatiotemporal distribution. Figure 4(b) shows the statistical analysis of the wind differences between the result of scanning lidar and the 10-frame result of the wind camera. The mean difference is close to 0, and the standard deviation (SD) is 0.42 m/s.

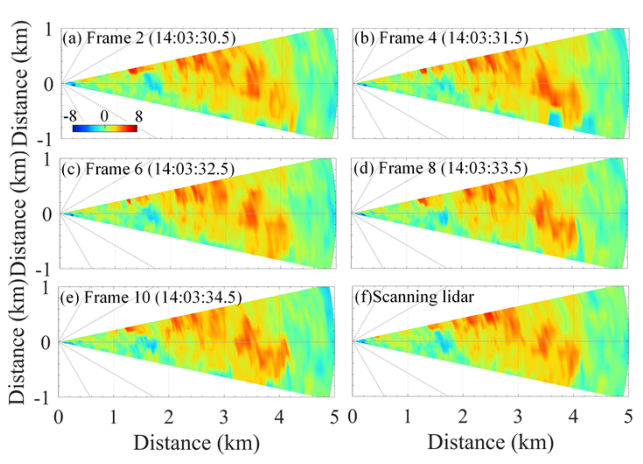


Fig. 5. (a)–(e) Typical imaging results of variable wind field and (f) the corresponding result of scanning lidar.

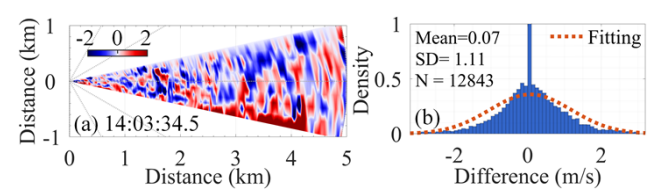


Fig. 6. LOSV difference distribution for the case of variable wind field. (a) LOSV differences between scanning lidar and the wind camera. (b) Probability density distribution of the wind differences.

Figure 5 shows the comparison results of the two lidars for the case of a variable wind field at 14:03, local time. There is a windshear zone with a speed of 8 m/s at the range of 2–4 km. By comparing the results of different frames of the wind camera, it can be found that the wind speed texture structure has obvious distortion with time, and there is also an obvious difference with the scanning result. The windshear in this area changes rapidly, driven by turbulence.

Figure 6(a) shows the LOSV difference distribution for the case of variable wind field. There is a significant wind difference between the results of scanning the lidar and the first frame result of the wind camera in the entire scanning area. Specifically, the last beam has the highest difference for the greatest time-lag effect. These wind differences will cause great interference to windshear identification.

Compared with Fig. 4(b), the probability density distribution of wind difference in Fig. 6(b) is more discrete. The SD reaches 1.11 m/s. The proportion of wind difference exceeding 1 m/s and 2 m/s is 25.1% and 7.5%, respectively. Therefore, for high variable wind fields, the time-lag effect of scanning lidar is exacerbated and cannot be ignored. The wind camera has significant advantages in detecting such variable wind fields.

In order to compare the measurement ability of the two types of lidar for atmospheric turbulence spectrum, the LOSV at 10 detection nodes with the same radial distance of R=240~m is adopted for energy spectrum analysis, as shown in Figs. 7(a) and 7(b). The distance between detection nodes is 12.6 m. In the process of scanning, the turbulence field evolves, producing time ambiguity for the rapidly changing small-scale turbulence. Thus, the sequence LOSV texture of the wind camera is clearer than that of the scanning lidar.

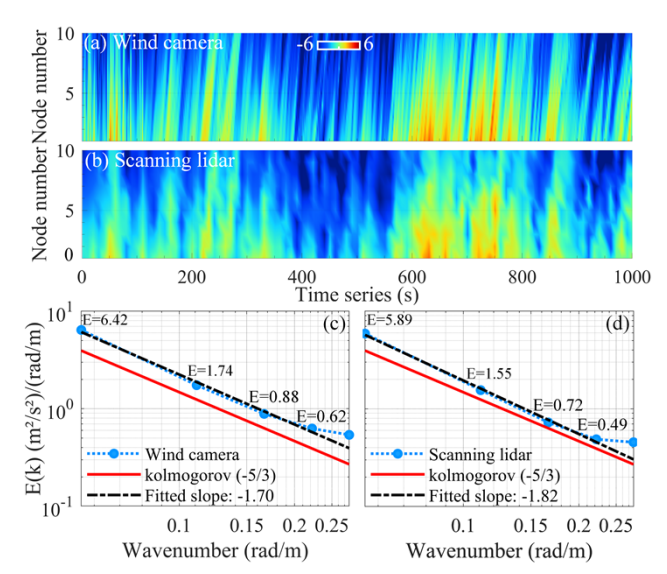


Fig. 7. (a), (b) LOSV series of wind camera and scanning lidar. (c), (d) Turbulence energy spectrum of scanning lidar and wind camera.

Spatial turbulence energy spectrum analysis results of the two types of lidar are shown in Figs. 7(c) and 7(d). The wave number κ is defined as $\kappa=2\pi/\lambda$, with λ being the wavelength of the atmospheric fluctuation. When κ values are 0.11 rad/m, 0.17 rad/m, and 0.22 rad/m, the energies of the scanning lidar are 89.0%, 81.9%, and 77.6% of that of the wind camera. The energy attenuation of the scanning lidar significantly intensifies with the increase in wave number (the decrease of spatial scale). Small-scale turbulence dominated by viscous dissipation changes faster over time, and the time-lag during scanning makes it unable to capture small-scale structures at the same moment, leading to significant energy attenuation. Larger-scale turbulence changes slower over time, and the time-sharing error of the scanning lidar is relatively small. Fortunately, the wind camera retains energy more completely across all scales.

According to the locally isotropic turbulent hypotheses of Kolmogorov theory, the energy spectrum of turbulence obeys the –5/3 power law in the inertial sub-range. Linear fitting of energy spectrum results measured using the wind camera and scanning lidar is conducted. The spectral slope of the scanning lidar is –1.82, which deviates significantly from the theoretical value with an error of 9.2%. The steep slope indicates that time-sharing sampling seriously affects small-scale energy measurement. The spectral slope of the wind camera is –1.70, which is highly consistent with the theoretical value of the Kolmogorov spectrum with an error of 2.0%, indicating that its synchronous sampling can accurately capture the inertial sub-region characteristics of turbulence. Therefore, the wind

camera can effectively capture the turbulent energy cascade and is more suitable for scenes requiring small-scale measurement.

In summary, a wind camera is demonstrated to image the transient wind field. In contrast to traditional scanning lidars, it eliminates measurement errors caused by time-lag effects. Thus, it exhibits superiority in terms of detection accuracy and temporal resolution when measuring rapidly changing wind fields. If sacrificing maximum range is permitted, the detection frame rate can be increased even with this prototype system. Furthermore, the data collected by the system highly adhere to the frozen turbulence hypothesis, providing a foundation for high-precision inversion of 2D wind fields. In terms of turbulent spatial spectrum measurement, the wind camera also outperforms scanning lidars—particularly in capturing the characteristics of the inertial sub-range—rendering it more suitable for high-resolution turbulence monitoring. In the current system, all laser emission ends are arranged in a line on the focal plane of the camera. So, horizontal wind field was captured in real time. A matrix of laser ends (10×10) will be equipped onto the focal plane, allowing 3D transient wind field recording in the near future.

Funding. National Natural Science Foundation of China (42405137); Natural Science Foundation of Jiangsu Province (BK20230434).

Disclosures. The authors declare no conflicts of interest.

Data availability. Data underlying the results presented in this paper are not publicly available at this time but may be obtained from the authors upon reasonable request.

REFERENCES

- 1. X. Huang, J. Zheng, A. Shao, et al., Atmos. Res. 311, 107680 (2024).
- 2. J. Yuan, L. Su, H. Xia, et al., Remote Sens. 14, 1626 (2022).
- 3. J. Yuan, H. Xia, T. Wei, et al., Opt. Express 28, 37406 (2020).
- 4. J. Li, C. Shen, H. Gao, et al., Opt. Express 28, 4286 (2020).
- H. Gao, C. Shen, Y. Zhou, et al., IEEE Geosci. Remote Sens. Lett. 19, 1 (2022).
- H. Xu, D. Sun, Y. Wu, et al., IEEE Trans. Geosci. Remote Sens. 61, 1 (2023).
- 7. Y. Zhang, Y. Wu, and H. Xia, Opt. Lett. 46, 5550 (2021).
- 8. Y. Zhang, J. Yuan, Y. Wu, et al., Phys. Rev. Fluids 8, L022701 (2023).
- 9. X. Zhang, K. Wang, Z. Lin, et al., Appl. Opt. 63, 3250 (2024).
- 10. H. Xia, Y. Chen, J. Yuan, et al., Remote Sens. 16, 924 (2024).
- 11. H. Tsuji, N. Kotake, S. Kameyama, et al., Opt. Lett. 49, 2890 (2024).
- N. Kotake, H. Sakamaki, M. Imaki, et al., Opt. Express 30, 20038 (2022).
- A. Choukulkar, R. Calhoun, B. Billings, et al., IEEE Geosci. Remote Sens. Lett. 9, 1132 (2012).
- 14. P. W. Chan and A. M. Shao, Meteorol. Z. 16, 491 (2007).
- J. Rye and R. Hardesty, IEEE Trans. Geosci. Remote Sens. 31, 16 (1993).